Charge-Density Ripples Modulated by Nuclear Quantum Effects in High-Harmonic Generation in Solids

Shi-Qi Hu,[1] Qing Chen,[1,2] and Sheng Meng[1,2,3,*]

[1]Beijing National Laboratory for Condensed Matter Physics and Institute of Physics, Chinese Academy of Sciences, Beijing 100190, People's Republic of China

[2]School of Physical Sciences, University of Chinese Academy of Sciences, Beijing 100049, People's Republic of China

[3]Songshan Lake Materials Laboratory, Dongguan, Guangdong 523808, People's Republic of China

(Received 1 July 2025; revised 3 February 2026; accepted 23 February 2026; published 30 March 2026)

Nuclear quantum effects (NQEs) significantly influence many fundamental physical and chemical phenomena. However, their impact on ultrafast dynamics remains poorly understood. Here, we demonstrate that solid-state high-harmonic generation (HHG) provides a promising platform for probing NQEs in attosecond processes. In particular, NQEs substantially modify HHG trajectories due to charge density ripples (CDR) induced by nuclear quantum delocalization. Incorporating NQE-modulated CDR shifts the oscillation phase of HHG, and thus introduces special properties and measurable signatures in the harmonic features, including the emission symmetry and rotation angle of the harmonic polarization ellipse, providing a plausible explanation for recent experimental observations. These findings enable all-optical detection of NQE-driven charge fluctuations via HHG spectroscopy.

DOI: 10.1103/8v2p-j9m4

Nuclear quantum effects (NQEs), such as zero-point vibrations and quantum tunneling of atoms [1–6], emerge to make a significant impact on many fundamental physical and chemical phenomena, thereby affecting a variety of material properties. These effects include quantum lattice stabilization, quantum paraelectricity, and superconductivity [4–6]. In contrast, the impact of NQEs on the dynamic processes—particularly those occurring at ultrafast timescales—remains poorly understood. Given the fact that quantum distribution of nuclear wave function and nuclear delocalization could alter the atomic structure and potential energy surface, NQEs are expected to play a profound role in the dynamic processes in solids.

Nevertheless, even in well-studied molecular systems, the exploration of NQEs in ultrafast processes—such as photoionization and charge migration [7–10]—remains in its infancy, let alone in solids. Understanding the role of NQEs is thus crucial for gaining insights into various novel quantum phenomena in attosecond science, including decoherence and entanglement [10–12]. Moreover, given that lasers are now a key tool for preparing quantum states, studying NQEs in ultrafast dynamics could potentially offer new solutions for quantum state manipulation in quantum computing and communication [13–15].

As a prominent area of ultrafast science, solid-state high-harmonic generation (HHG) arises from coherent collisions between delocalized charge carriers and the lattice potential [16–20], a process highly sensitive to NQEs. In this Letter, we demonstrate the significant and previously overlooked influence of NQEs on the oscillation phase and angular distribution of HHG in graphene, providing a plausible explanation for the anomalous ellipticity of HHG observed in recent experiments [19,20], which remains an open question. While previous studies phenomenologically revealed the dephasing effects on HHG ellipse [20], this dephasing model fails under high laser intensities. In contrast, we reveal a fundamentally distinct and direct physical picture that is conceptually distinct from dephasing. This mechanism stems from the modulation of charge density ripples (CDR)—spatial fluctuations in the charge density distribution around nuclei—induced by nuclear quantum delocalization. The NQE-modulated CDR acts as an effective polarization that alters the trajectory of electrons undergoing nonlinear scattering by the lattice potential. The results enable an all-optical probe of NQE-induced charge density redistribution via HHG.

The influence of NQEs on HHG has been investigated in monolayer graphene [Fig. 1(a)], which serves as a prototype system where strong NQEs of carbon atoms significantly affect the structural, vibrational, elastic and thermal properties [21–24]. Ring-polymer molecular dynamics (RPMD) and *ab initio* molecular dynamics (AIMD) are employed at different temperatures (50–500 K) to account for NQEs and classical thermal effects [25–28], respectively. In our study, the zero-point vibration of C nuclei constitutes the main NQEs which is not included in AIMD but well described by RPMD [21,24,38]. The RPMD accounts for zero-point vibration using a set of replicas of the system, which are coupled together by harmonic

*Contact author: smeng@iphy.ac.cn

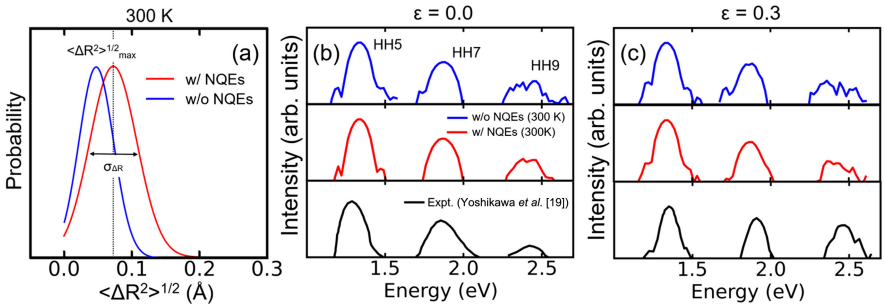

FIG. 1. Probability distributions of C nuclei delocalization in graphene $\langle \Delta R^2 \rangle^{1/2}$, without (a) and with NQEs (b) at 300 K. The distribution peaks (labeled by black dotted lines) are the most probable nuclei delocalization $\langle \Delta R^2 \rangle^{1/2}_{\max}$ and $\sigma_{\Delta R}$ is the delocalization width. HHG spectra of graphene with and without NQEs under lasers with ellipticity $\varepsilon = 0.0$ (b) and $\varepsilon = 0.3$ (c). The experimental data are taken from Ref. [19].

interactions, to simulate the effect of a nuclear wave packet based on Feynman's path integral approach [21,24,38]. These effects were incorporated by sampling the distorted lattice configurations generated from multiple molecular dynamics trajectories [27,28].

To study HHG, we combine AIMD and RPMD with first-principles time-dependent density-functional theory (TDDFT) simulations [39–41]. An elliptical polarized laser pulse with Gaussian envelope electric field $\boldsymbol{F}(t) = \boldsymbol{F}_0(1+\varepsilon^2)^{-1/2}\exp(-(t-t_0)^2/2\sigma^2)(\cos\omega t, \varepsilon\sin\omega t)$ is adopted in the graphene plane with $\omega \sim 0.26$ eV, $\sigma \sim 28.0$ fs, $t_0 = 100$ fs, and $\boldsymbol{F}_0 \sim 0.2$ V/Å. Here, ε is the ellipticity. By adding the vector potential $\boldsymbol{A}(t) = -c\int \boldsymbol{F}(t')dt'$ in the Hamiltonian and evolving the electronic wave functions in real time, the HHG spectra are obtained through the Fourier transform of time-dependent current $\boldsymbol{j}(t) = (1/2i)\int dr[\psi^*(r,t)\nabla\psi(r,t) + \text{c.c.}]$ [28,39,40].

Figure 1(a) shows the probability distributions of nuclear delocalization $\langle \Delta R^2 \rangle^{1/2}$ of C atoms in graphene with NQEs and with classical thermal effects only (without NQEs). The distribution peaks indicate the most probable nuclear delocalization $\langle \Delta R^2 \rangle^{1/2}_{\max}$ while $\sigma_{\Delta R}$ represents the delocalization width. Here, $\langle \Delta R^2 \rangle^{1/2} = \langle \Delta R_x^2 + \Delta R_y^2 + \Delta R_z^2 \rangle^{1/2}$, where $\Delta R_{x,y,z}$ denotes the nuclear displacement induced by either NQEs or classical thermal effects along different directions, following a Gaussian distribution centered around the equilibrium position.

Because of the high zero-point energy of C atoms (~0.1 eV), zero-point vibration—whose vibration frequency can surpass its thermal energy by an order of magnitude even at room temperature (300 K)—produce a large superposition of nuclear wave packets, significantly enhancing nuclear delocalization. Consequently, $\langle \Delta R^2 \rangle^{1/2}_{\max}$ increases from 0.04 Å (without NQEs) to 0.07 Å (with NQEs), while $\sigma_{\Delta R}$ changes from 0.05 to 0.08 Å when NQEs are included.

The corresponding HHG spectra of graphene under both linear ($\varepsilon = 0.0$) and elliptical ($\varepsilon = 0.3$) polarized laser are shown in Figs. 1(b) and 1(c), comparing cases with and without NQEs. Compared to the classical framework (without NQEs), the inclusion of NQEs suppresses the noisy splits appearing in HHG peaks, resulting in clearer better-resolved spectra. This effect is particularly evident for higher harmonics (e.g., the 9th harmonic), consistent with recent experimental observations [19].

More importantly, NQEs significantly affect the polarization ellipse of HHG radiation, as shown in Figs. 2(a) and 2(b), zero-point vibration of C modify the rotation angle θ_{HHG} of the HHG polarization ellipse—defined as the angle between the major axis of the harmonic polarization and that of the fundamental laser field. In particular, when NQEs are included, the θ_{HHG} of the 5th and 7th harmonics exhibit rotations of approximately 50° and 52°, respectively, in good agreement with recent experimental results where $\theta^{\text{expt.}} \sim 60°$ [19].

The θ_{HHG} of the 5th and 7th harmonics are plotted as functions of laser ellipticity ε in Figs. 2(c) and 2(d). The θ_{HHG} in both classical (without NQEs) and quantum (with NQEs) cases shows a similar ε dependence. However, the θ_{HHG} difference between classical and quantum framework, i.e., $\Delta\theta_{\text{HHG}} = \theta_{\text{HHG}}^{\text{w/NQE}} - \theta_{\text{HHG}}^{\text{w/o NQE}}$, becomes increasingly pronounced at higher laser ellipticities [Figs. 2(c)–2(f)] and lower temperatures (see Supplemental Material, Fig. S4 [28]). Laser ellipticity affects both the electron paths and excitation-induced dephasing during the HHG dynamics. Through prior work links $\Delta\theta_{\text{HHG}}$ to dephasing effects [20], in our study the laser ellipticity is found to mainly modify the electron paths while having a minimal impact on excitation probability and thus the excitation-induced dephasing (as shown in Fig. S10 [28]). The dependence of $\Delta\theta_{\text{HHG}}$ on ε here suggests the potential contribution of a distinct new mechanism: the electron dynamical trajectories play important roles on the NQE-modulated HHG.

To explore the mechanism of NQEs on electron dynamical trajectories in HHG, Fig. 3 shows the snapshot of the spatial fluctuations of charge density distribution $\Delta\rho$ at the field-peaking time of laser pulse, induced by either zero-point vibrations or classical thermal effects, respectively. The $\Delta\rho$,

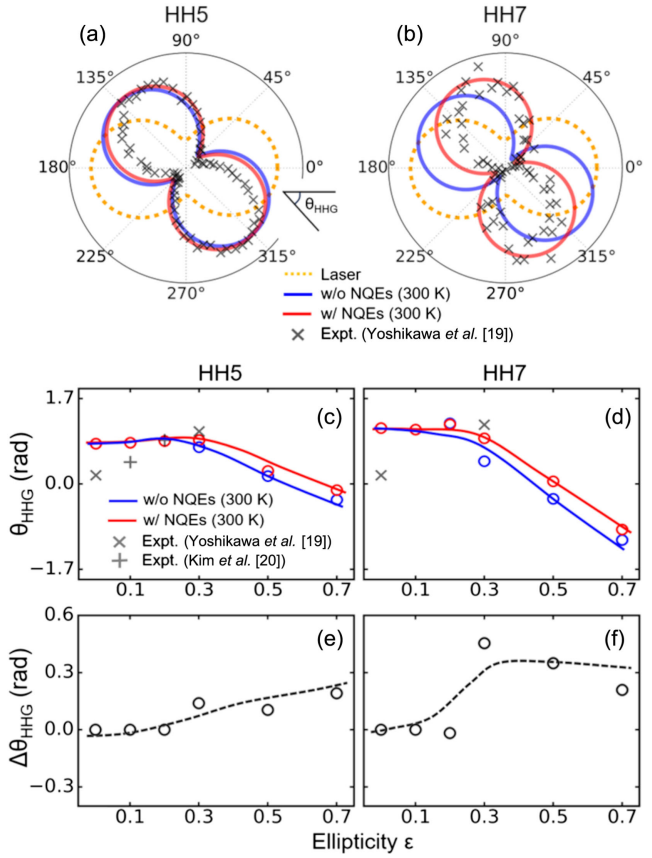

FIG. 2. Polar plots of normalized intensities for the 5th (a) and 7th (b) harmonic under $\varepsilon = 0.3$ laser with and without NQEs. Orange dashed lines indicate the laser intensity profile, while gray crosses denote experimental data from Ref. [19]. Rotation angle θ_{HHG} for the 5th (c) and 7th (d) harmonic as functions of ellipticity, comparing cases with and without NQEs. Gray crosses show experimental data from Refs. [19,20], with solid lines serving as guides to the eye. Rotation angle differences $\Delta\theta_{\mathrm{HHG}} = \theta_{\mathrm{HHG}}^{\mathrm{w/NQE}} - \theta_{\mathrm{HHG}}^{\mathrm{w/o\ NQE}}$ for the 5th (e) and 7th (f) harmonic versus ellipticity. Black dashed lines display fitting results from the scattering model.

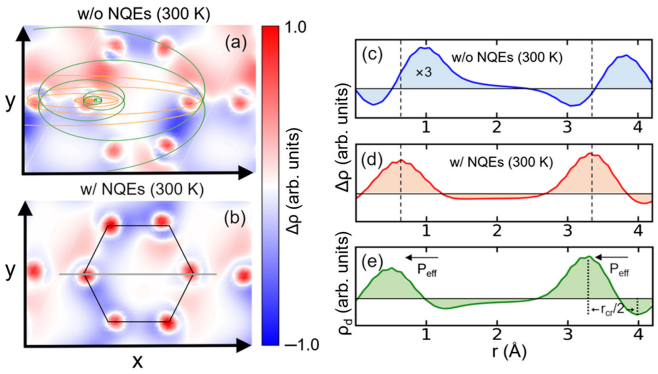

FIG. 3. The snapshot of charge density ripples (the spatial fluctuations of charge density distribution $\Delta\rho$) in graphene plane at the field peaking time of laser pulse induced by (a) classical thermal effects (w/o NQEs) and (b) NQEs. The green (yellow) curve labels the electron trajectory in real space driven by laser field with ellipticity $\varepsilon = 0.7$ ($\varepsilon = 0.2$). The black hexagon outlines a carbon hexagonal ring. The charge density ripples along the C-C bond direction [marked by solid gray line in (b)] induced by (c) classical thermal effect (w/o NQEs) and (d) NQEs. Black dashed lines mark carbon atom positions; solid black lines denote $\Delta\rho = 0$. For comparison, the value of $\Delta\rho$ without NQEs in (a) and (c) is multiplied by 3.0. (e) The charge density ripples difference $\rho_{\mathrm{d}} = \Delta\rho^{\mathrm{w/NQE}} - \Delta\rho^{\mathrm{w/o\,NQE}}$. The black arrows schematize the effective polarization drived by charge density ripples. The r_{cr} represnts average spatial length of the effective polarization.

which we call CDR, is the charge density difference between that with an ideal undistorted lattice and that with structural distortions due to either zero-point vibrations (with NQEs) or classical thermal fluctuations (without NQEs). As shown in Figs. 3(a) and 3(b), within the classical framework, the CDR snapshot displays an anisotropic distribution centered around C nuclei equilibrium positions. This anisotropy originates from instantaneous thermal fluctuations of graphene and may average out in the long-time duration.

In contrast, zero-point vibrations introduce substantial nuclear delocalization that dramatically reshapes both the potential energy surface and electronic structure. These quantum effects not only amplify charge fluctuations, but also produce a more homogeneous, symmetric charge distribution around C nuclei almost at each moment. This NQE-driven transition in CDR is robust across various temperatures (Supplemental Material, Fig. S5 [28]) and is clearly evident in the $\Delta\rho$ profile along C-C bond directions [Figs. 3(c) and 3(d)]. As shown in Fig. 3(e), the NQE-mediated CDR reorganization—quantified by $\Delta\rho$ difference, $\rho_{\mathrm{d}} = \Delta\rho^{\mathrm{w/NQE}} - \Delta\rho^{\mathrm{w/o\,NQE}}$—acts as an effective polarization P_{eff} that effectively eliminates the thermal CDR anisotropy.

Compared to the classical case (without NQEs), similar to the dynamic core polarization of solid HHG [42], the NQE-modulated CDR alters electron dynamical trajectories and consequently affects HHG through the effective polarization P_{eff}. Within the real-space scattering framework [16], solid-state HHG arises from nonlinear electron scattering by the periodic lattice potential. For a laser field $\boldsymbol{F}_L(t) = \boldsymbol{F}_0 \sin(\omega t)$, the harmonics originate from the time derivative of the induced current $(\partial/\partial t)\boldsymbol{j}(t)$, which is governed by the charge-density-dependent lattice potential $V(r)$: $(\partial/\partial t)\boldsymbol{j}(t) \propto -\boldsymbol{\nabla}\sum_{\boldsymbol{k}} V_{\boldsymbol{k}} \mathrm{e}^{(-i\boldsymbol{k}\boldsymbol{r}(t))} = i\sum_{\boldsymbol{k}} \boldsymbol{k} V_{\boldsymbol{k}} \mathrm{e}^{\{-i\boldsymbol{k}[-(\boldsymbol{F}_0/m\omega^2)\sin(\omega t)]\}}$. Here k and $V_{\boldsymbol{k}}$ represent reciprocal lattice vectors and Fourier components of the lattice potential, respectively. The electron trajectory within a unit cell follows the laser electric field as $\boldsymbol{r}(t) = -(\boldsymbol{F}_0/m\omega^2)\sin(\omega t)$. Applying the Jacobi-Anger expansion and considering the spatial inversion symmetry of graphene, the N th-order harmonic current ($N = 2n - 1$) in the classical regime (without NQEs) oscillates as $(\partial/\partial t)\boldsymbol{j}_N(t) \propto \sum_{\boldsymbol{k}} \boldsymbol{k} V_{\boldsymbol{k}} J_N(\boldsymbol{k}\boldsymbol{F}_0/m\omega^2)\sin(N\omega t)$, where J_N

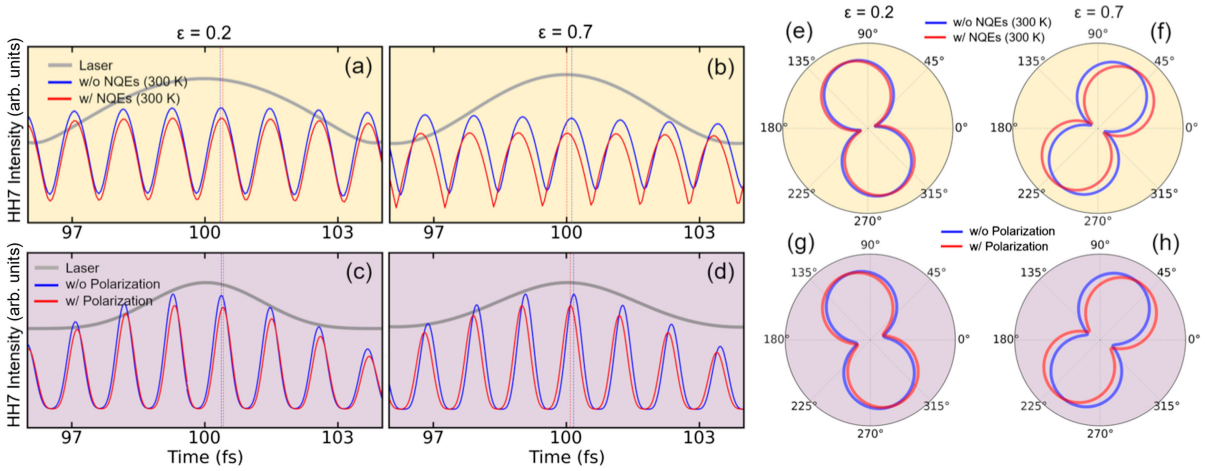

FIG. 4. The time oscillation of the 7th harmonic under $\varepsilon = 0.2$ (a) and $\varepsilon = 0.7$ (b) laser excitation, comparing cases with and without NQEs. Corresponding oscillations from the scattering model with and without CDR-induced effective polarization are shown for $\varepsilon = 0.2$ (c) and $\varepsilon = 0.7$ (d) lasers. Gray solid lines indicate the laser field profile, while blue dashed and red dashed lines represent harmonic phases without and with NQEs and effective polarization, respectively. Polar plots of normalized intensities of the 7th harmonic for $\varepsilon = 0.2$ (e) and $\varepsilon = 0.7$ (f) laser, comparing cases with and without NQEs. Corresponding polar normalized intensities from scattering model with and without CDR-induced polarization for $\varepsilon = 0.2$ (g) and $\varepsilon = 0.7$ (h) laser. Panels (a), (b), (e), (f) present TDDFT calculations, while (c), (d), (g), (h) show scattering model results.

is the Bessel function of the first kind of order N. The corresponding HHG intensity is given by $I_N = \sum_{\boldsymbol{k}} \boldsymbol{k} V_{\boldsymbol{k}} J_N(\boldsymbol{k}\boldsymbol{F}_0/m\omega^2)$.

In the NQE regime, however, the effective polarization P_{eff} acting on HHG can be treated as an additional periodic potential with an average characteristic length r_{cr} [Fig. 3(e)], expressed as $V_{\text{eff}}(r) = V_P e^{(-2\pi i r(t)/r_{\text{cr}})}$. The modified current of the Nth harmonic trajectory becomes $I_N \sin(N\omega t) - I'_N \sin(N\omega t)$ where the additional term $I'_N = V_P(2\pi/r_{\text{cr}}) J_N(2\pi \boldsymbol{F}_0/r_{\text{cr}} m\omega^2)$. For our system, the HHG intensity modulation I'_N induced by P_{eff} is quite small compared to the 5th and 7th harmonics intensities (Supplemental Material, Fig. S6 [28]), i.e., $I'_N \ll I_N$. Thus, we can approximate $(\partial/\partial t)\boldsymbol{j}_N(t) \propto I_N[\sin(N\omega t) - (I'_N/I_N)\sin(N\omega t)] = I_N[\sin(N\omega t) - \sin\beta_N \sin(N\omega t)]$, where $\sin\beta_N \approx \beta_N = (I'_N/I_N)$ for $(I'_N/I_N) \sim 0$. This expression can be reformulated as $(\partial/\partial t)\boldsymbol{j}_N(t) \propto I_N[A_N + B_N \sin(N\omega t + \Delta\varphi_{\text{HHG}})]$, with $\Delta\varphi_{\text{HHG}} = (\beta_N/2) + (\pi/8)$, $A_N = (\sqrt{2}-1) \times \sin[N\omega t - (\pi/4)]$ and $B_N = 2\cos[(\beta_N/2) + (3\pi/8)]$. These results demonstrate that the CDR modulated by zero-point vibration of C introduces an additional phase shift $\Delta\varphi_{\text{HHG}}$ in the HHG temporal oscillation. Since the polar plot rotation angle θ_{HHG} reflects the harmonic oscillation timing [$\theta_{\text{HHG}} \propto N\omega t$, Figs. 4(a), 4(b), 4(e), and 4(f)], the phase shift $\Delta\varphi_{\text{HHG}}$ directly corresponds to the observed angular change $\Delta\theta_{\text{HHG}}$. This mechanism fully explains the NQE-induced rotation of polarization ellipse of HHG shown in Figs. 2(a) and 2(b).

This scenario is further validated through direct comparison between TDDFT trajectories and the real-space scattering model described above. Figures 4(a) and 4(b) display the time oscillation of the 7th harmonic signal under different laser ellipticity, comparing cases with and without NQEs. The corresponding angular distribution of harmonic polarization ellipse is shown in polar plots in Figs. 4(e) and 4(f). Compared to the classical case, zero-point vibrations introduce both a phase shift $\Delta\varphi_{\text{HHG}}$ in the harmonic oscillation and a corresponding rotation $\Delta\theta_{\text{HHG}}$ of the polarization ellipse. As ellipticity increases (from $\varepsilon = 0.2$ to 0.7), the magnitude of $\Delta\varphi_{\text{HHG}}$ (and consequently $\Delta\theta_{\text{HHG}}$) grows while its direction reverses. Remarkably, the scattering model incorporating the effective polarization successfully reproduces all key influences of NQEs on HHG dynamics [Figs. 4(c), 4(d), 4(g), and 4(h)], achieving quantitative reconstruction of both the magnitudes and variation trends of $\Delta\varphi_{\text{HHG}}$ and $\Delta\theta_{\text{HHG}}$.

This mechanism further explains the ellipticity dependence of $\Delta\theta_{\text{HHG}}$. As ellipticity increases, electron dynamical trajectories sample more regions of effective polarization within the graphene lattice [Fig. 3(a)], thereby enhancing the modulation of HHG dynamics and consequently $\Delta\theta_{\text{HHG}}$. On the other hand, the harmonic intensity I_N decreases with the increasing ellipticity, especially for $\varepsilon \geq 0.3$ (as shown in Fig. S6 in Supplemental Material [28]). Since the phase shift $\Delta\varphi_{\text{HHG}} \propto (I'_N/I_N)$, reduction in I_N gives more significant $\Delta\varphi_{\text{HHG}}$ ($\Delta\theta_{\text{HHG}}$) at larger ε value.

Using the established relationship $\Delta\varphi_{\text{HHG}} \propto [I'_N/I_N(\varepsilon)]$ where $I'_N = V_P(2\pi/r_{\text{cr}}) J_N(2\pi \boldsymbol{F}_0/r_{\text{cr}} m\omega^2)$ and $I_N(\varepsilon)$ is derived from harmonic spectra, we fit the $\Delta\theta_{\text{HHG}}$ versus ellipticity ε dependence [the black dash lines in Figs. 2(e) and 2(f)] and estimate the average characteristic length $r_{\text{cr}} \sim 1.6$ Å for P_{eff}, showing good agreements with the CDR difference results in Fig. 3(e). Given that r_{cr} corresponds to the spatial size of charge redistribution induced

by zero-point vibration, these results imply that HHG spectroscopy can be a direct probe for the characteristic length of charge fluctuations induced by NQEs.

Given the universality of zero-point vibrations, we extended our study to various materials. We consistently found that NQEs significantly modify HHG spectra and polarization (Fig. S7 [28]), demonstrating their broad applicability. More profoundly, NQEs can further alter HHG selection rules and polarization outcomes under circular excitation (Fig. S12 [28]), suggesting their role in generating diverse and tunable HHG phenomena.

In conclusion, solid-state HHG has emerged as a promising platform for exploring NQEs such as zero-point vibration in attosecond processes. This includes how NQEs affect the HHG trajectory by modulating the CDR and providing an effective polarization. These vital and fundamental quantum effects, in turn, shift the oscillation phase of HHG and thus introduce novel properties and measurable signatures in the emission features of harmonics, including the selection rules, emission symmetry, and rotation angle of the harmonic polarization ellipse, which are well observed in recent experiments [19,20]. Investigations into these features enable the direct probing of NQE-induced charge fluctuations, thereby providing insights into the future of attosecond quantum science.

Acknowledgments—We acknowledge financial support from Ministry of Science and Technology (Grant No. 2021YFA1400200), National Natural Science Fund of China (Grants No. 12450401 and No. 12025407), and Chinese Academy of Sciences (No. YSBR047). S.-Q. H. acknowledges financial support from National Natural Science Fund of China (No. 12304096), China Postdoctoral Science Foundation (2022TQ0362), and Special Research Assistant of the Chinese Academy of Sciences Foundation.

Data availability—The data that support the findings of this article are openly available [43].

[1] T. Markland *et al.*, Nuclear quantum effects enter the mainstream, Nat. Rev. Chem. **2**, 0109 (2018).
[2] M. Ceriotti, W. Fang, P. G. Kusalik, R. H. McKenzie, A. Michaelides, M. A. Morales, and T. E. Markland, Nuclear quantum effects in water and aqueous systems: Experiment, theory, and current challenges, Chem. Rev. **116**, 7529 (2016).
[3] W. Chu, S. Tan, Q. Zheng, W. Fang, Y. Feng, O. V. Prezhdo, B. Wang, X.-Z. Li, and J. Zhao, Ultrafast charge transfer coupled to quantum proton motion at molecule/metal oxide interface, Sci. Adv. **8**, eabo2675 (2022).
[4] I. Errea, M. Calandra, C. J. Pickard, J. R. Nelson, R. J. Needs, Y. Li, H. Liu, Y. Zhang, Y. Ma, and F. Mauri, Quantum hydrogen-bond symmetrization in the superconducting hydrogen sulfide system, Nature (London) **532**, 81 (2016).
[5] I. Errea *et al.*, Quantum crystal structure in the 250-kelvin superconducting lanthanum hydride, Nature (London) **578**, 66 (2020).
[6] K. A. Müller and H. Burkard, $SrTiO_3$: An intrinsic quantum paraelectric below 4 K, Phys. Rev. B **19**, 3593 (1979).
[7] D. T. Matselyukh, V. Despré, N. V. Golubev, A. I. Kuleff, and H. J. Wörner, Decoherence and revival in attosecond charge migration driven by non-adiabatic dynamics, Nat. Phys. **18**, 1206 (2022).
[8] C. Bourassin-Bouchet, L. Barreau, V. Gruson, J. F. Hergott, F. Quere, P. Salieres, and T. Ruchon, Quantifying decoherence in attosecond metrology, Phys. Rev. X **10**, 031048 (2020).
[9] D. Dey, A. I. Kuleff, and G. A. Worth, Quantum interference paves the way for long-lived electronic coherences, Phys. Rev. Lett. **129**, 173203 (2022).
[10] L. Cruz-Rodriguez, D. Dey, A. Freibert, and P. Stammer, Quantum phenomena in attosecond science, Nat. Rev. Phys. **6**, 691 (2024).
[11] A. S. Maxwell, L. B. Madsen, and M. Lewenstein, Entanglement of orbital angular momentum in non-sequential double ionization, Nat. Commun. **13**, 4706 (2022).
[12] M. J. J. Vrakking, Control of attosecond entanglement, and coherence, Phys. Rev. Lett. **126**, 113203 (2021).
[13] M. A. Nielsen and I. L. Chu, *Quantum Computation and Quantum Information* (Cambridge University Press, Cambridge, England, 2010).
[14] A. K. Ekert, Quantum cryptography based on Bell's theorem, Phys. Rev. Lett. **67**, 661 (1991).
[15] D. Bouwmeester, J.-W. Pan, K. Mattle, M. Eibl, H. Weinfurter, and A. Zeilinger, Experimental quantum teleportation, Nature (London) **390**, 575 (1997).
[16] H. Lakhotia, H. Y. Kim, M. Zhan, S. Hu, S. Meng, and E. Goulielmakis, Laser picoscopy of valence electrons in solids, Nature (London) **583**, 55 (2020).
[17] E. Goulielmakis and T. Brabec, High harmonic generation in condensed matter, Nat. Photonics **16**, 411 (2022).
[18] Y. You, D. A. Reis, and S. Ghimire, Anisotropic high-harmonic generation in bulk crystals, Nat. Phys. **13**, 345 (2017).
[19] N. Yoshikawa, T. Tamaya, and K. Tanaka, High-harmonic generation in graphene enhanced by elliptically polarized light excitation, Science **356**, 736 (2017).
[20] Y. Kim, M. J. Kim, S. Cha, S. Choi, C.-J. Kim, B. J. Kim, M.-H. Jo, J. Kim, and J. D. Lee, Dephasing dynamics accessed by high harmonic generation: Determination of electron–hole decoherence of Dirac fermions, Nano Lett. **24**, 1277 (2024).
[21] C. P. Herrero and R. Ramirez, Quantum effects in the structural and elastic properties of graphite: Path-integral simulations, Phys. Rev. B **104**, 054113 (2021).
[22] C. P. Herrero *et al.*, Nuclear quantum effects in graphene bilayers, J. Chem. Phys. **28**, 204707 (2019).
[23] C. P. Herrero and R. Ramírez, Nuclear quantum effects in graphane, Chem. Phys. **533**, 110737 (2020).
[24] H. Jiang, X. Tao, M. Kammler, F. Ding, A. M. Wodtke, A. Kandratsenka, T. F. Miller, and O. Bünermann, Small nuclear quantum effects in scattering of H and D from graphene, J. Phys. Chem. Lett. **12**, 1991 (2021).
[25] S. Habershon, D. E. Manolopoulos, T. E. Markland, and T. F. Miller, III ring-polymer molecular dynamics: Quantum

effects in chemical dynamics from classical trajectories in an extended phase space, Annu. Rev. Phys. Chem. **64**, 387 (2013).

[26] I. R. Craig and D. E. Manolopoulos, Quantum statistics and classical mechanics: Real time correlation functions from ring polymer molecular dynamics, J. Chem. Phys. **121**, 3368 (2004).

[27] D. Freeman, A. Kheifets, S. Yamada, A. Yamada, and K. Yabana, High-order harmonic generation in semiconductors driven at near- and mid-infrared wavelengths, Phys. Rev. B **106**, 075202 (2022).

[28] See Supplemental Material at http://link.aps.org/supplemental/10.1103/8v2p-j9m4 for more details, which includes Refs. [29–37].

[29] S. Q. Hu, H. Zhao, X. B. Liu, Q. Chen, D. Q. Chen, X. Y. Zhang, and S. Meng, Phonon-coupled high-harmonic generation for exploring nonadiabatic electron-phonon interactions, Phys. Rev. Lett. **133**, 156901 (2024).

[30] M. X. Guan, S. Hu, H. Zhao, C. Lian, and S. Meng, Towards attosecond control of electron dynamics in two-dimensional materials, Appl. Phys. Lett. **116**, 043101 (2020).

[31] S. Q. Hu, D.-Q. Chen, L.-L. Du, and S. Meng, Solid-state high harmonic spectroscopy for all-optical band structure probing of high-pressure quantum states, Proc. Natl. Acad. Sci. U.S.A. **121**, e2316775121 (2024).

[32] G. Kresse and J. Hafner, *Ab initio* molecular-dynamics for open-shell transition-metals, Phys. Rev. B **48**, 13115 (1993).

[33] M. Ceriotti, J. More, and D. E. Manolopoulos, i-PI: A Python interface for *ab initio* path integral molecular dynamics simulations, Comput. Phys. Commun. **185**, 1019 (2014).

[34] V. Kapil *et al.*, i-PI 2.0: A universal force engine for advanced molecular simulations, Comput. Phys. Commun. **236**, 214 (2019).

[35] M. Ceriotti, G. Bussi, and M. Parrinello, Nuclear quantum effects in solids using a colored-noise thermostat, Phys. Rev. Lett. **103**, 030603 (2009).

[36] M. Ceriotti and D. E. Manolopoulos, Efficient first-principles calculation of the quantum kinetic energy and momentum distribution of nuclei, Phys. Rev. Lett. **109**, 100604 (2012).

[37] V. Korolev *et al.*, Unveiling the role of electron-phonon scattering in dephasing high-order harmonics in solids, arXiv:2401.12929.

[38] I. R. Craig and D. E. Manolopoulos, Quantum statistics and classical mechanics: Real time correlation functions from ring polymer molecular dynamics, J. Chem. Phys. **121**, 3368 (2004).

[39] C. Lian, S.-Q. Hu, M.-X. Guan, and S. Meng, Momentum-resolved TDDFT algorithm in atomic basis for real time tracking of electronic excitation, J. Chem. Phys. **149**, 154104 (2018).

[40] S. Meng and E. Kaxiras, Local basis-set and real time implementation of time-dependent density-functional theory for excited state dynamics simulations, J. Chem. Phys. **129**, 054110 (2008).

[41] R. J. Zhao, P. W. You, and S. Meng, Ring Polymer Molecular Dynamics with Electronic Transitions, Phys. Rev. Lett. **130**, 166401 (2023).

[42] L. Li *et al.*, Dynamic core polarization in high harmonic generation from solids: The example of MgO crystals, Phys. Rev. Lett. **126**, 187401 (2021).

[43] S. Hu *et al.*, Data for this study, Zenodo, Version 1, 2026, 10.5281/zenodo.18854641.